Chandra X-Ray Observations of V830 Tau: A T Tauri Star Hosting an Evanescent Planet

Stephen L. Skinner[1] and Manuel Güdel[2]

[1] Center for Astrophysics and Space Astronomy (CASA), Univ. of Colorado, Boulder, CO, 80309-0389, USA; stephen.skinner@colorado.edu
[2] Dept. of Astrophysics, Univ. of Vienna, Türkenschanzstr. 17, A-1180 Vienna, Austria

Received 2021 May 3; revised 2021 June 24; accepted 2021 July 2; published 2021 October 8

Abstract

The radial velocity study by Donati et al. (2016) reported the detection of a close-in giant planet in a 4.93 day orbit around the ∼2 Myr old weak-lined T Tauri star V830 Tau. Because of the stringent timescale constraints that a very young host star like V830 Tau would place on hot-Jupiter formation models and inward-migration mechanisms, independent confirmation of the planet's existence is needed but so far has not been obtained. We present new Chandra X-ray observations of V830 Tau. The Chandra observations in combination with previous XMM-Newton observations reveal strong, variable X-ray emission with an X-ray luminosity spanning the range $\log L_x = 30.10$–30.87 erg s^{-1}. Chandra High Energy Transmission Grating spectra show emission lines formed over a range of plasma temperatures from ∼4 MK (Ne IX) to ∼16 MK (S XV). At the separation of the reported planet (0.057 au) the X-ray flux is $\sim 10^6$–10^7 times greater than the Sun's X-ray flux at Jupiter. We provide estimates of the X-ray ionization and atmospheric heating rates at the planet's separation and identify areas of uncertainty that will need to be addressed in any future atmospheric models.

Unified Astronomy Thesaurus concepts: T Tauri stars (1681); X-ray stars (1823); stars: individual (V830 Tau)

1. Introduction

Hot Jupiters Around Solar-Like Stars: The discovery of a Jupiter-mass planet in a 4.2 day orbit around the ∼6 Gyr old solar-like star 51 Peg by Mayor & Queloz (1995) was not anticipated given the absence of close-in giant planets in our own solar system. As a result of ongoing searches for new exoplanets, many such massive exoplanets in short-period orbits have now been discovered, mostly around older stars. Such "hot Jupiters" typically have masses of $M_p \geqslant 0.25~M_J$ (where M_J is Jupiter's mass) and orbital periods of $P_{\rm orb} \lesssim 10$ days, as reviewed by Dawson & Johnson (2018). The mechanism(s) by which such massive planets form and end up so close to the host star is still debated. Some models posit in situ formation at close separation but a more prevalent idea is that they form at several astronomical units beyond the frost line and migrate inward. The planet's inward migration and ultimate destruction by a death spiral into the star or tidal breakup is blocked, likely a result of star–planet–disk interactions involving angular-momentum exchange, magnetic fields, and tidal effects (Strugarek et al. 2017; Dawson & Johnson 2018).

Recent observational studies are providing tantalizing evidence for the presence of hot Jupiters orbiting much younger, solar-mass pre-main-sequence T Tauri stars (TTSs). The reported detections are based on radial velocity (RV) studies which are challenging since they require the faint, periodic planetary RV signal to be recovered in the presence of contamination from strong stellar magnetic activity. Of primary interest here is the ∼2 Myr old weak-lined TTS V830 Tau (Table 1) for which a massive planet has been reported in a 4.93 day orbit (Donati et al. 2015, 2016, 2017). A hot Jupiter has also been reported orbiting the ∼17 Myr old weak-lined TTS TAP 26 (V1069 Tau) with a period of 9–11 days and best-fit value $P_{\rm orb} = 10.79$ days (Yu et al. 2017). Planets have also been reported around other TTSs but at much larger separations than for hot Jupiters. Perhaps the most compelling example is the detection of one or more directly imaged formative planets around the classical TTS LkCa 15 at separations of $a \approx 15$–20 au (Kraus & Ireland 2012; Sallum et al. 2015). LkCa 15 is a strong X-ray source but the planets are well-shielded from high-energy stellar radiation by intervening disk gas (Skinner & Güdel 2013, 2017).

Hot Jupiters orbiting TTSs are crucial for developing an understanding of how exoplanets form, and obviously place tight constraints on the timescale for any inward migration. They are also excellent laboratories for studying the effects of stellar X-ray and EUV (XUV) heating on the planet's atmosphere and photoevaporative mass loss. The XUV luminosity of TTSs is enhanced by orders of magnitude relative to their older main-sequence counterparts. As a result of intense XUV irradiation, mass loss models from hot Jupiters orbiting TTSs must take radiative heating and cooling into account (Murray-Clay et al. 2009; Owen & Jackson 2012).

V830 Tau and its Evanescent Planet: Extended spectropolarimetric and photometric observations of the weak-lined TTS V830 Tau in late 2015 and early 2016 revealed periodic RV variations that were attributed to a close-in giant planet, V830 Tau b (Donati et al. 2015, 2016, 2017). The observations were obtained using the 3.6 m Canada–France–Hawaii Telescope and 8 m Gemini North Telescope with the ESPaDOnS high-resolution spectropolarimeter and a similar spectrometer on the 2 m Télescope Bernard Lyot. The authors reported that strong magnetic activity was observed and filtered out in order to characterize the planet's RV signature. The orbital period based on all data was determined to be $P_{\rm orb} = 4.927 \pm 0.008$ days and a separation of $a = 0.057 \pm 0.001$ au, about seven times smaller than Mercury's semimajor axis. The lower limit on the planet's mass is $M_p \sin(i) = 0.57~M_J$, or $M_p = 0.70 \pm 0.12~M_J$ assuming $i = 55°$. In the absence of a photometric transit detection, the planet's radius is not known. At an age of ∼2 Myr, a giant planet orbiting V830 Tau would make it the youngest star so far known to host a hot Jupiter.

Table 1
V830 Tau: Stellar Properties

Sp. Type	Age (Myr)	M_* ($M_\odot$)	R_* ($R_\odot$)	$T_{\rm eff}$ [a] (K)	L_* ($L_\odot$)	$P_{\rm rot}$ (d)	A_V (mag)	Distance (pc)
K7 (1,2)	≈2.2 (2)	1.00 ± 0.05 (2)	2.0 ± 0.2 (2)	≈4090 (1,2)	1.2 ± 0.3 (2)	2.741 (3)	0.4 (1)	130.4 ± 0.3 (4)

Notes.
[a] The quoted value is the average of 3930 K for type K7.5 (ref. 1) and 4250 K for type K7 (ref. 2).
References—(1) Herczeg & Hillenbrand (2014); (2) Donati et al. (2015); (3) Grankin et al. (2008); and (4) Gaia EDR3.

An attempt to confirm the RV detection of V830 Tau b was undertaken by Damasso et al. (2020). Their independent study was carried out between 2017–2020 using the HARPS-N echelle spectrograph mounted on the 3.6 m Telescope Nazionale Galileo. Somewhat surprisingly, they did not confirm the suspected 4.93 day RV variations. However, they note that their non-detection does not conclusively rule out the existence of V830 Tau b since an increased level of stellar magnetic activity during their observing period would make it more difficult to recover the faint planetary signal. Nevertheless it is clear that further observational monitoring of V830 Tau will be needed to verify the planet's existence.

Our interest in this system arises from the strong, variable X-ray emission of V830 Tau which was detected in a 2005 XMM-Newton observation with the star captured far off-axis (Franciosini et al. 2007). Their model fits of the XMM-Newton spectra revealed high plasma temperatures of $T \gtrsim 33$ MK, as commonly found in magnetically active, late-type coronal X-ray sources. The star's surface magnetic field was mapped by Donati et al. (2017) who also detected optical flares. Other signs of magnetic activity include highly variable, nonthermal radio emission (Bower et al. 2016). The planet's close separation raises the possibility that its orbital motion could perturb the star's magnetic field structure and induce flares through tidal effects or star–planet magnetic interactions. Although a study of mostly main-sequence G–M exoplanet host stars by Poppenhaeger et al. (2010) found no conclusive evidence for effects on coronal X-ray emission (as measured by L_x/L_{bol}) due to star–planet interactions, V830 Tau is much younger and TTS tend to be much more magnetically active and X-ray luminous than older late-type, main-sequence stars.

Keck interferometer *JHK* observations of V830 Tau showed no significant near-IR excess (Akeson et al. 2005). Remarkably, within a timespan of ∼2 Myr the inner disk has been cleared, leaving any close-in planet directly exposed to harsh XUV radiation from the star. But it is noteworthy that the Keck interferometric observations weakly resolved V830 Tau in the *K* band. Several possible explanations were proposed by Akeson et al. (2005) including an unknown companion in the 50 mas field of view or an extended component of stellar scattered light. This raises the interesting question of whether a close-in giant planet might have affected the *K*-band interferometry.

We present here new Chandra observations of V830 Tau which provide the information on its X-ray properties needed to model planet-irradiation effects. We provide estimates of X-ray ionization and heating rates and identify areas of uncertainty that will need to be addressed in any future models of the planet's atmosphere.

Table 2
Summary of V830 Tau Chandra Observations[a]

Parameter				
ObsId	21166	21962	21963	21964
Start Date (2018)/	Nov	Nov	Nov	Nov
Time (TT)	15/10:53	16/15:41	17/03:31	18/01:09
Stop Date (2018)/	Nov	Nov	Nov	Nov
Time (TT)	15/17:59	16/22:41	17/10:27	18/07:47
Elapsed Time (s)	25,568	25,214	24,986	23,879
Livetime (s)[b]	22,949	22,789	22,792	21,715

Notes.
[a] Data were obtained using ACIS-S/HETG in faint timed event mode, a frame time of 3.1 s, and with CCD chips S1-S5 enabled. The nominal roll angle for all observations was 107°.16. The average X-ray centroid position of V830 Tau from all four observations was (J2000) R.A. = 04h33m10s.02, decl. = +24°33′43″.0 which is offset by only 0″.29 from the Gaia EDR3 position R.A. = 04h33m10s.04, decl. = +24°33′42″.9.
[b] Livetime corresponds to the time during which source data were being collected and excludes operational and instrumental overheads such as CCD readout times.

2. X-Ray Observations

As summarized in Table 2, Chandra observed V830 Tau in four observations acquired in 2018 November using the Advanced CCD Imaging Spectrometer (ACIS-S) and High-Energy Transmission Grating (HETG) spectrometer. The total observing time was split into four observations of roughly equal duration as a result of Chandra's operational and thermal constraints.

The data were reduced using the Chandra Interactive Analysis of Observations (CIAO version 4.11) software in combination with CALDB version 4.8.2 calibration data.[3] Separate spectra and X-ray light curves were generated for each observation in order to search for source variability, and variability was detected. X-ray spectra and associated response matrix files and auxiliary response files files were extracted using CIAO *specextract*. Energy-filtered light curves were produced using CIAO *dmextract*. Undispersed (zero-order) spectra and light curves were extracted from a circular region of radius 1″.5 centered on the source peak. Background and pileup were negligible. The spectra were analyzed using XSPEC version 12.10.1 and CIAO *Sherpa's* spectral-analysis tools.

3. Results

3.1. Undispersed X-Ray Light Curves and Spectra

V830 Tau was clearly detected in all four Chandra observations, as summarized in Table 3. Significant count rate

---

[3] Further information on CIAO and CALDB can be found at https://cxc.cfa.harvard.edu.

Table 3
Summary of V830 Tau's X-Ray Properties (ACIS-S zero-order)[a]

ObsId	Rate (c ks^{-1})	Counts (c)	H.R.	E_{50} (keV)	kT_{wgtd} (keV)	$F_{\mathrm{x,abs}}$ (erg cm^{-2} s^{-1})	log L_x (erg s^{-1})
21166	5.71 ± 1.65	134	0.28	1.28	1.10[b]	4.70 ± 0.44e-13[b]	30.10[b]
21962	6.00 ± 2.31	141	0.35	1.63	1.84	5.51 ± 0.53e-13	30.16
21963[c]	9.08 ± 6.70v	212	0.36	1.61	1.61	7.47 ± 0.59e-13[d]	30.29
21964	11.8 ± 3.3	270	0.47	1.90	2.08	9.70 ± 0.81e-13	30.40
mean	8.15		0.36	1.60	1.66	6.84e-13	30.25

Notes.

[a] Mean count rate (Rate), counts, H.R., median event energy (E_{50}), absorbed X-ray flux ($F_{\mathrm{x,abs}}$), and unabsorbed X-ray luminosity (L_x, evaluated at $d = 130.4$ pc) are computed using events in the 0.2–8 keV range. H.R. = counts(2–8 keV)/counts(0.2–8 keV). A "v" denotes significant count rate variability during the observation. The count-rate uncertainties are 1σ. The values of the weighted plasma temperature kT_{wgtd}, $F_{\mathrm{x,abs}}$, and L_x were determined from 2T *apec* thermal plasma models with a fixed absorption of $N_H = 8 \times 10^{20}$ cm^{-2} and metallicity of $Z = 0.4\, Z_{\odot}$, except for ObsId 21166 where a 1T *apec* model gave an acceptable fit. For the 2T *apec* models, the value of kT_{wgtd} is determined by weighting the contribution of each temperature component by its respective XSPEC *norm*, or equivalently by its volume emission measure (EM).
[b] Fit parameters are based on a 1T *apec* model.
[c] Fits of the high-state spectrum (Figure 2) using 143 events from the last 8.77 ks of the observation with a 2T *apec* model give k$T_{\mathrm{cool}} = 0.6(\pm 0.3)$ keV, k$T_{\mathrm{hot}} = 2.4(\pm 0.7)$ keV, k$T_{\mathrm{wgtd}} = 1.7$ keV, $F_{\mathrm{x,abs}} = 14.3(\pm 1.6) \times 10^{-13}$ erg cm^{-2} s^{-1}, and log $L_x = 30.58$ erg s^{-1}.
[d] A Gaussian component at $E = 1.473$ keV was included in the spectral model used to fit the full ObsId 21963 spectrum (low + high states). This component improves the fit to a spectral feature that is most likely the Mg XII doublet ($E_{\mathrm{lab}} = 1.473$ and 1.472 keV) which is visible in Figure 2.

variability was detected only in ObsId 21963, for which the CIAO *glvary* statistical test gives a probability of variability $P_{\mathrm{var}} > 0.999$ based on the arrival times of events in the 0.2–8 keV energy range. The X-ray light curve (Figure 1) shows an increase in count rate occurring ≈ 15 ks after the start of ObsId 21963. The mean count rate was 4.92 c ks^{-1} during the first 14 ks (low state) and 16.3 c ks^{-1} during the last 8.8 ks (high state) of the observation. The hardness ratio defined as H.R. = counts(2–8 keV)/counts(0.2–8 keV) was H.R. = 0.22 during the first segment and H.R. = 0.43 during the second segment. A comparison of the low-state and high-state ACIS-S zero-order spectra is shown in Figure 2. No significant variability was found in the other three observations, but the count rate and observed flux in the last observation (ObsId 21964) were about twice as high than in the first two observations.

The source clearly became brighter during the 2.87 day interval over which the four observations were obtained. Since the 2.87 day interval spanned by all four observations covers only one stellar rotation period and 58% of the planet's 4.93 day orbital period reported by Donati et al. (2017), additional time monitoring over multiple cycles would be needed to determine if the X-ray variability is tied to the rotational or orbital periods.

The combined zero-order spectrum consisting of events from all four observations is shown in Figure 3 (top). Since the source varied over the course of the observations, the spectrum of each observation was fitted separately. The ACIS-S zero-order spectra were acceptably fitted with single-temperature (1T) or two-temperature (2T) thermal *apec* plasma models (Smith et al. 2001), as summarized in Table 3. The spectra do not have sufficient counts to reliably determine the absorption column density so it was held fixed at the value $N_H = 8 \times 10^{20}$ cm^{-2} corresponding to $A_V = 0.4$ mag, and the conversion $N_H = 2 \times 10^{21} A_V$ cm^{-2} as obtained by averaging the results of Gorenstein (1975) and Vuong et al. (2003).

The fits summarized in Table 3 use a metallicity fixed at $Z = 0.4\, Z_{\odot}$ since the higher-resolution grating spectra suggest some important metals such as Fe have subsolar abundances (Section 3.2). The undispersed CCD spectra do not tightly constrain the metallicity, which is sensitive to the temperature of the hot-plasma component (kT_2). A simultaneous fit of the ACIS-S spectra for the first two observations where no significant variability was detected allow values $Z = (0.34–1.3)\, Z_{\odot}$ (1σ range), with smaller values of Z corresponding to larger values of kT_2. The assumed value of Z has very little effect on the value of L_x determined from the fits of the undispersed CCD spectra.

The first observation (ObsId 21166) has the softest spectrum and lowest observed flux, and it was acceptably fitted using a 1T *apec* model with a temperature of k$T = 1.10 \pm 0.08$ keV. During the remaining three observations the source flux and spectral H.R. increased. These three observations were better fitted with 2T *apec* models which gave k$T_1 \approx 0.7$ keV and k$T_2 \approx 2.2–3.8$ keV. The last observation (ObsId 21964) shows the hardest spectrum (H.R. = 0.47) and its flux at energies above ≈ 2 keV is higher than the other three observations.

The results in Table 3 for ObsId 21963 when the source varied are based on all 212 events for the full observation. In addition, separate spectra were extracted for the first 14 ks during low state (69 counts) and last 8.8 ks during high state (143 counts). In low state the observed flux was $F_{\mathrm{x,abs}}(0.2–8$ keV$) = 6.4(\pm 1.3) \times 10^{-13}$ erg cm^{-2} s^{-1} which increased to $14.3(\pm 1.6) \times 10^{-13}$ erg cm^{-2} s^{-1} in high state.

There are insufficient counts in the low-state spectrum to obtain a reliable temperature measurement. Fits of the high-state spectrum with 2T *apec* models (Table 3; notes) yield a hot-component temperature of $T_{\mathrm{hot}} = 28(\pm 8)$ MK. This value of T_{hot} and the $\approx 9–10$ ks decay time of the outburst are similar to those reported for the V830 Tau flare detected by XMM-Newton ($T_{\mathrm{peak}} \geqslant 33$ MK, $\tau_{\mathrm{decay}} = 11.4$ ks; Franciosini et al. 2007). By comparison, much more powerful flares have been detected in TTs in the Taurus, Orion, and Rho Ophiuchi star-forming regions with decay times $\tau_{\mathrm{decay}} \sim 100$ ks and $T_{\mathrm{peak}} \sim 100$ MK (Imanishi et al. 2003; Franciosini et al. 2007; Getman et al. 2008).

The ACIS-S zero-order spectra show possible weak emission lines or blended lines, most noticeable in the 0.9–1 keV range from Ne IX and Ne X which are clearly visible in the MEG1 grating spectrum (Figure 3). Line emission is discussed further in the grating analysis section below.
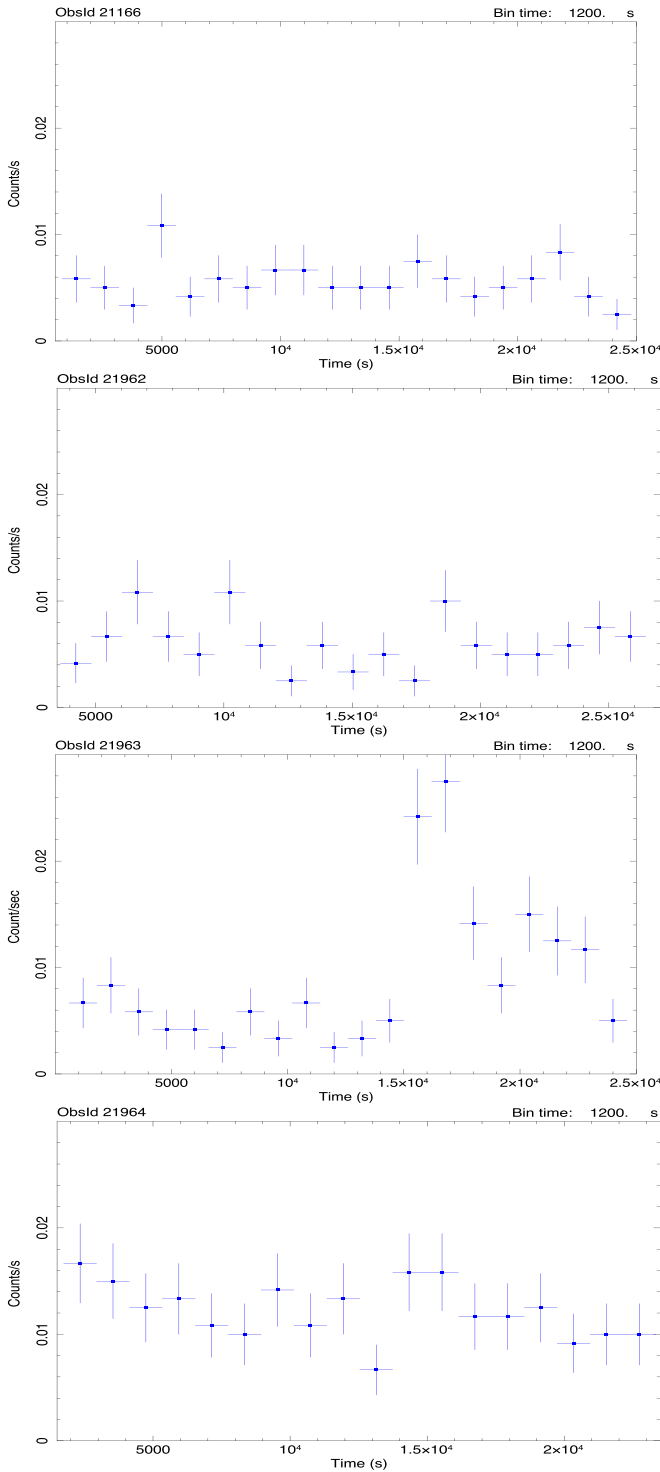
Figure 1. Chandra ACIS-S zero-order light curves of V830 Tau (0.2–8 keV) showing variability in ObsId 21963. All plots use the same y-axis scale. Times are relative to the start of each Chandra observation (Table 2).

The mean intrinsic X-ray luminosity determined from the ACIS-S zero-order fits at the Gaia EDR3 distance of 130.4 pc is $\log L_x(0.2\text{--}8 \text{ keV}) = 30.25$ erg s^{-1} but varied over the range 30.10–30.40 erg s^{-1} (Table 3). Fits to the Chandra grating spectra allow slightly higher L_x values (Section 3.2). The previous XMM-Newton observations measured a decline in the X-ray luminosity of V830 Tau from $\log L_x = 30.87$ to 30.39 erg s^{-1} with an e-folding time of 11.4 ks, where we have

adjusted the L_x values reported by Franciosini et al. (2007) to $d = 130.4$ pc. The low end of the L_x range from XMM-Newton observations overlaps the Chandra range and taken together the observations imply that L_x can vary by at least 0.77 dex.

3.2. Grating Spectra

All four MEG1 spectra were combined into a summed spectrum to bring out faint line emission, as shown in Figure 3 (top). The brightest line detections are summarized in Table 4, focusing mainly on ObsIds 21963 and 21964 (Figure 3; bottom) which had higher count rates. Because of the low number of counts in each line, the line widths were held fixed at MEG1's instrumental resolution (FWHM $\Delta\lambda = 0.023$ Å) when fitting the lines with Gaussian profiles.

The lowest energy line is a possible detection of O VII at $E_{\rm lab} = 0.574$ keV (21.602 Å) which has maximum line power at $\log T_{\rm max} = 6.3$ (K) and is visible in ObsId 21963 (Figure 3 bottom). This feature is too faint for a reliable flux measurement and is thus not included in Table 4.

The strongest lines are the Ne IX He-like triplet resonance line at $E_{\rm lab} = 0.922$ keV (13.447 Å) shown in Figure 4 and the Ne X line at $E_{\rm lab} = 1.022$ keV (12.132 Å). Neither line shows any significant centroid shift. Fitting the MEG1 spectrum of ObsId 21964 using a fixed-width Gaussian profile gives $E_{\rm fit} = 0.919$ (± 0.001) keV for Ne IXr and $E_{\rm fit} = 1.021$ (± 0.002) keV for Ne X.

In addition to the Ne IXr line, the Ne IXf forbidden line (0.905 keV) is detected (ObsId 21964), but not the inter-combination line Ne IXi (0.915 keV). ObsId 21964 shows the highest Ne IX flux and a three-component Gaussian fit gives a relative flux normalization of the resonance to forbidden line ratio $r/f = 1.66/1.18 = 1.41$. The i-line flux normalization is consistent with zero. Thus, no indication of a suppressed flux ratio $R = f/i$ that can result from high electron densities is present. No significant flux was detected for the Mg XI or Si XIII triplets in the individual observations but a measurement of the summed $r+i+f$ fluxes in the combined MEG1 spectrum (Table 4) indicates that Mg XI emission is present as well as weaker emission from Si XIII. The highest temperature lines detected are Si XIV ($E_{\rm lab} = 2.006$ keV) and S XV ($E_{\rm lab} = 2.461$ keV), both of which have a maximum line power at $T_{\rm max} = 15.8$ MK. There is also weak emission at S XV in the combined ACIS zero-order spectrum (Figure 3; top).

There are insufficient counts in the MEG1 spectra of the individual observations to obtain useful abundance constraints. Thus the combined spectrum (785 net counts) using data from all four observations was fitted using a 2T vapec variable abundance model. The abundances of elements with detected emission lines (Ne, Mg, Si, S, and Fe) were allowed to vary either individually or in combination, but the abundance of each element was constrained to be equal for the cool- and hot-plasma components. The abundances of other elements in the vapec model (C, N, O, Al, Ar, Ca, and Ni) were all held fixed at the same value, which was taken to be either solar or subsolar (values of 0.2 or 0.4 × solar were compared). The column density was held fixed at $N_{\rm H} = 8 \times 10^{20}$ cm^{-2}.

The results of several different variable abundance fits can be summarized as follows: (i) the abundances of the varied elements converged to subsolar values (most notably Fe), as was also generally found for TTSs in the Taurus molecular cloud observed in the XEST study (Güdel et al. 2007); (ii) the fit results were insensitive to the S abundance; (iii) the cool-
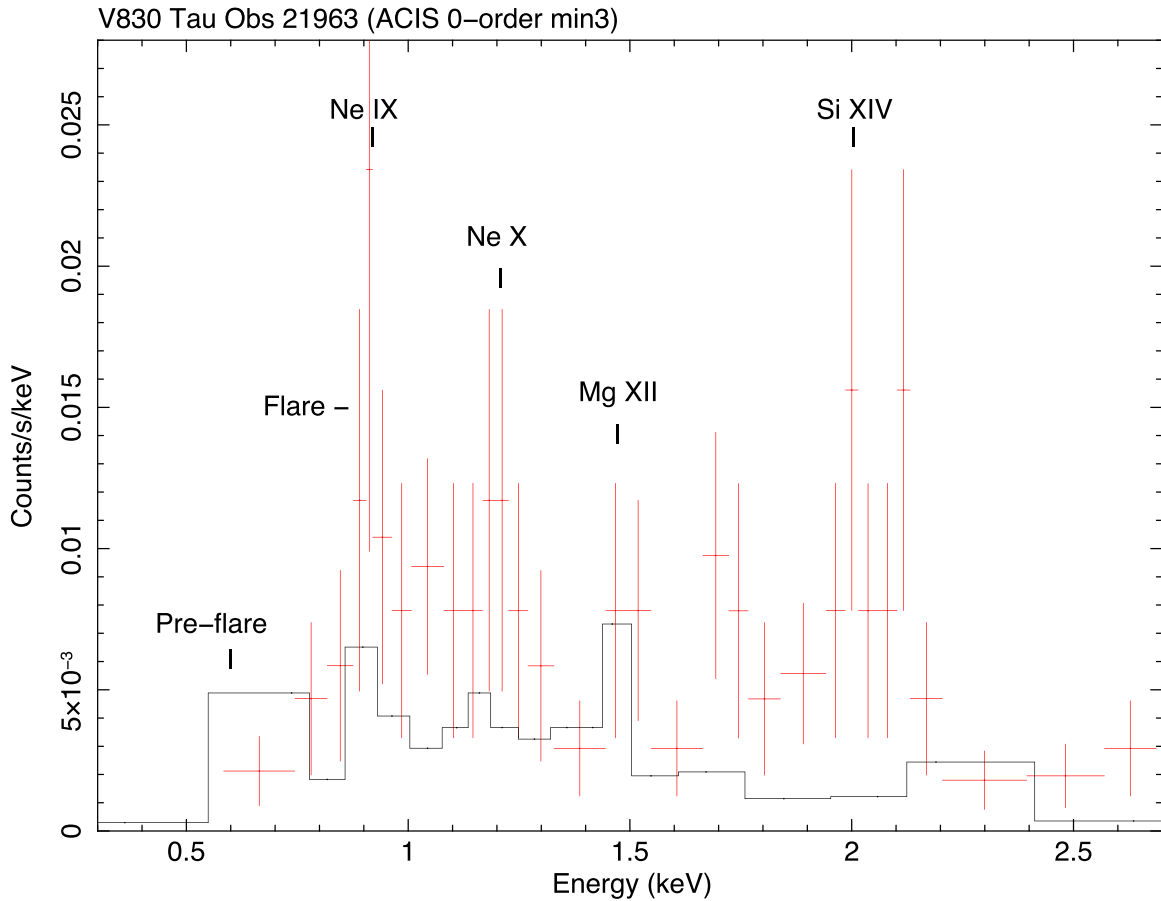
Figure 2. Comparison of the low-state (pre-flare, black) and high-state (flare, red) ACIS zero-order spectra of V830 Tau (ObsId 21963) lightly binned to a minimum of 3 counts per bin. The low-state spectrum includes 69 counts from the first 14.2 ks of usable exposure and the high-state spectrum is based on 143 counts from the last 8.77 ks. Candidate emission lines are identified. The feature at 1.473 keV is most likely weak Mg XII emission but it is not visible in the ObsId 21963 MEG1 spectrum.

and hot-plasma component temperatures ranged from $kT_{cool} = 0.37$–0.43 keV and $kT_{hot} = 2.0$–2.6 keV, respectively; (iv) the absorbed flux was in the range $F_{x,abs}(0.2$–8 keV$) = (1.1$–$1.2) \times 10^{-12}$ erg cm^{-2} s^{-1}; and (v) the luminosity range was log $L_x = 30.51$–30.59 erg s^{-1}. This L_x range is slightly above that obtained from fits of the ACIS-S CCD spectra and may reflect better accounting of line fluxes in the MEG1 spectrum. A representative 2T vapec variable abundance fit is summarized in Table 5.

4. Discussion

4.1. Comparison of V830 Tau with Other TTSs in Taurusp

Given the possible presence of a close-in planet orbiting V830 Tau it is appropriate to ask whether its X-ray luminosity is anomalous compared to other weak-lined TTSs. Using data acquired during the XMM-Newton Extended Survey of the Taurus Molecular Cloud (XEST), Telleschi et al. (2007) found a high probability of correlation between L_x and stellar luminosity L_* in TTSs. Using a Kaplan–Meier estimator that takes both detections and upper limits into account they obtained a mean value for weak-lined TTSs in the XEST sample of log$(L_x/L_*) = -3.36 \pm 0.07$.

To compare this with the Chandra observations of V830 Tau we use log $L_x = 30.42 \pm 0.17$ erg s^{-1} based on an average of the mean value obtained from the ACIS-S zero-order fits (Table 3) and the somewhat higher value obtained from the combined

MEG1 fit (Table 5). Taking $L_* = 1.2 \pm 0.3$ L$_\odot$ (Table 1) for V830 Tau gives log$(L_x/L_*) = -3.24$ $(-3.51, -2.96)$ where the range in parentheses accounts for the spread in L_x and the uncertainty of L_*. This value is slightly higher than the XEST mean by 1.7σ but the range in parentheses overlaps the XEST mean value. Thus, the Chandra observations of V830 Tau do not deviate significantly from the L_x/L_* ratio obtained from the XEST sample. On the other hand, the higher value of log $L_x = 30.87$ erg s^{-1} from the previous XMM-Newton observation gives log$(L_x/L_*) = -2.79$ which is 8.6σ higher than the XEST mean. So during periods of strong activity (e.g., flaring) V830 Tau's X-ray emission is well above the normal range for weak-lined TTSs in the Taurus molecular cloud.

4.2. X-ray Ionization and Heating

X-ray and EUV radiation ionizes and heats the planet's atmosphere. The X-ray ionization rate ζ at a given X-ray optical depth τ_x in the planet's atmosphere depends on the star's X-ray luminosity, plasma temperature kT_x, and separation a. The X-ray heating rate Γ_x depends on ζ and the planet's atmospheric properties, i.e., the number density n_H at the height where the heating rate is computed. Details on the calculations of the ionization and heating rates are given below.

Absorption of an X-ray photon of energy E by gas in the planet's atmosphere results in ionization and the production of a primary photoelectron having energy E—E_i, where E_i is the ionization potential. The primary photoelectron in turn
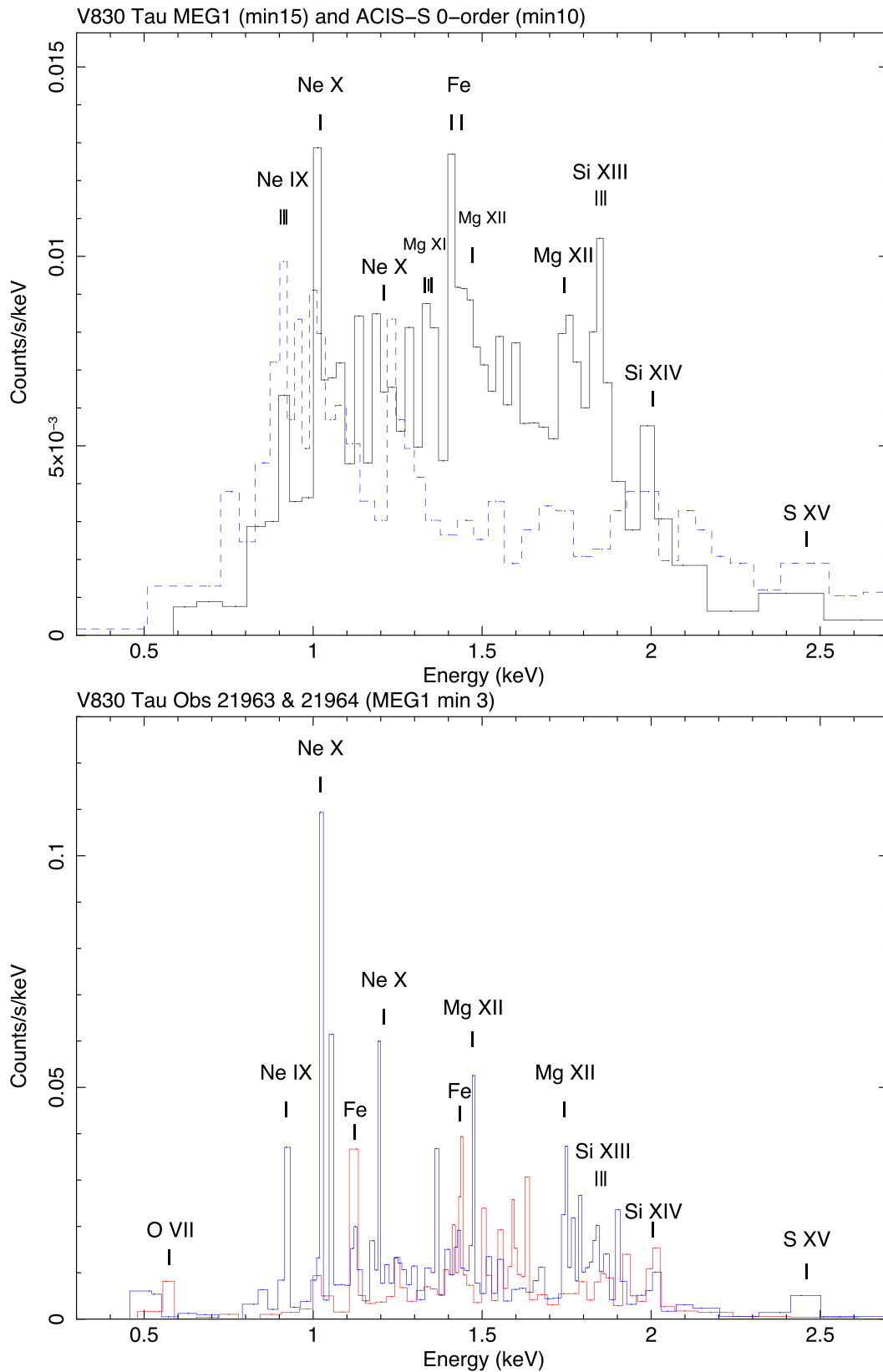
Figure 3. Top: Combined V830 Tau MEG1 spectrum of all four observations (solid line; 785 net counts) binned to a minimum of 15 counts per bin. For comparison, the combined ACIS-S zero-order spectrum is shown (dashed line; 757 net counts; 10 counts per bin). Error bars have been omitted for clarity. Bottom: Overlay of V830 Tau MEG first-order spectra (+1 and −1 orders combined) for ObsIds 21963 (red) and 21964 (blue) on a linear energy scale. The spectrum has been lightly binned in energy to a minimum of 3 counts per bin. Candidate emission lines with lab energies (keV) are O VII*r* (0.574), Ne IX*r* (0.922), Ne X (1.022 and 1.211), Fe XXIII/XXIV (1.124–1.129). Fe XXII/XXIII (1.423–1.439), Mg XII (1.473 and 1.745), Si XIIIrfi (1.865, 1.854, 1.839), Si XIV (2.006), and S XV (2.461). Error bars have been omitted for clarity.
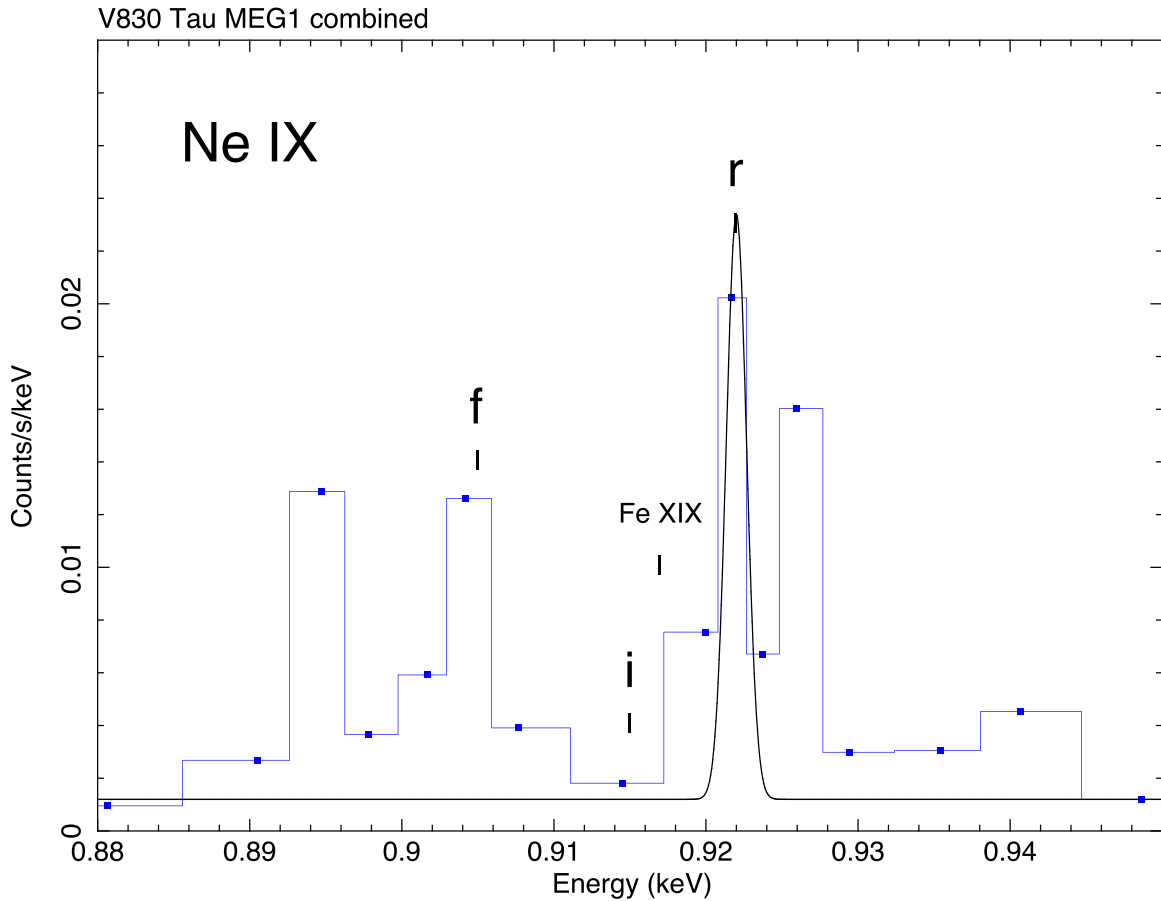
Figure 4. V830 Tau MEG first-order combined spectrum of the Ne IX He-like triplet using data from all four observations. The spectrum has been lightly binned to a minimum of 2 counts per bin. The vertical lines mark the lab energies of the resonance (r), intercombination (i), and forbidden (f) lines at $E_{lab} = 0.922, 0.915$, and 0.905 keV, respectively. The lab energy of Fe XIX (0.917 keV) is also shown. The Gaussian profile of the r line uses a fixed centroid energy of $E = E_{lab} = 0.922$ keV and FWHM = 0.67 eV corresponding to MEG1's spectral resolution. The i line is undetected. Error bars have been omitted for clarity.

Table 4
V830 Tau X-Ray Line Fluxes (MEG1)

Ion	E_{lab} (keV)	$\log T_{max}$ (K)	ObsId	Net Line Flux (10^{-6} ph cm^{-2} s^{-1})
Ne IX	0.922	6.6	21964	28.4 (15.3)[a,b]
Ne X	1.022	6.8	21166	15.4 (7.5)
Ne X	1.022	6.8	21964	15.1 (7.7)
Ne X	1.211	6.8	21166	3.3 (2.1)
Ne X	1.211	6.8	21962	2.5 (1.8)
Mg XI	1.352	6.8	sum[c]	4.4 (1.1)[a]
Mg XII	1.473	7.0	21964	3.3 (1.4)
Mg XII	1.745	7.0	21964	3.2 (1.2)
Si XIII	1.865	7.0	sum[c]	2.6 (0.6)[a]
Si XIV	2.006	7.2	21963	3.0 (1.3)
Si XIV	2.006	7.2	21964	2.1 (1.1)
S XV	2.461	7.2	21964	5.8 (2.8)

Notes. The laboratory energies (E_{lab}) and maximum line power temperatures (T_{max}) are from the ATOMDB database (www.atomdb.org). For He-like triplets (Ne IX, Mg XI, Si XIII) E_{lab} is for the resonance (r) line. Net photon (ph) line fluxes are continuum subtracted with uncertainties given in parentheses. The Gaussian line widths were held fixed at MEG1's spectral resolution (0.023 Å) during the fits.
[a] Sum of the triplet components: resonance (r) + intercombination (i) + forbidden (f) lines based on a three-component Gaussian fit.
[b] Triplet line fluxes are $r = 16.6$, $i \leqslant 1.5$, and $f = 11.8$.
[c] Only the summed spectrum of all four observations provided a measurable line flux. Thus, the quoted value is an average over the summed exposure of 90.245 ks (Table 2).

produces multiple secondary ionizations which dominate the X-ray heating. The X-ray photoelectric absorption cross section drops off rapidly with incident photon energy and is approximated by a power law $\sigma(E) = \sigma_0 \, (E/1 \text{ keV})^{-p} \text{ cm}^{-2}$, where we use $\sigma_0 = 2.27 \times 10^{-22} \text{ cm}^2$ and $p = 2.485$ as appropriate for solar-abundance gas (Igea & Glassgold 1999; Shang et al. 2002). If metals are depleted onto grains then the value of p must be adjusted (Glassgold et al. 1997).

The X-ray optical depth for a photon of energy E is related to the equivalent neutral H column density via $\tau_x = \sigma(E) N_H$ at a unit optical depth $N_H(\tau_x = 1) = 1/\sigma(E)$. For the median photon energy $E_{50} = 1.6$ keV of V830 Tau, the above relation gives $\tau_x = 1$ at $N_H = 1.4 \times 10^{22} \text{ cm}^{-2}$. If $n_H(z)$ is the number density at height z above the planet's surface then the corresponding column density is $N_H = \int n_H(z) dz$, where the integral is evaluated along the line of sight from the star to the target point in the atmosphere. An atmospheric model specifying $n_H(z)$ is needed to determine the height z corresponding to a given value of τ_x (Section 4.4).

At X-ray energies of $E \lesssim 3$ keV that are relevant for V830 Tau, scattering effects are negligible compared to photoelectric absorption and the scattering cross section can be ignored (Bruderer et al. 2009). Because of the steep decline of $\sigma(E)$ with energy, low-energy X-ray photons (and EUV photons) will be absorbed higher in the planet's atmosphere and the absorbed spectrum thus becomes harder and weaker with
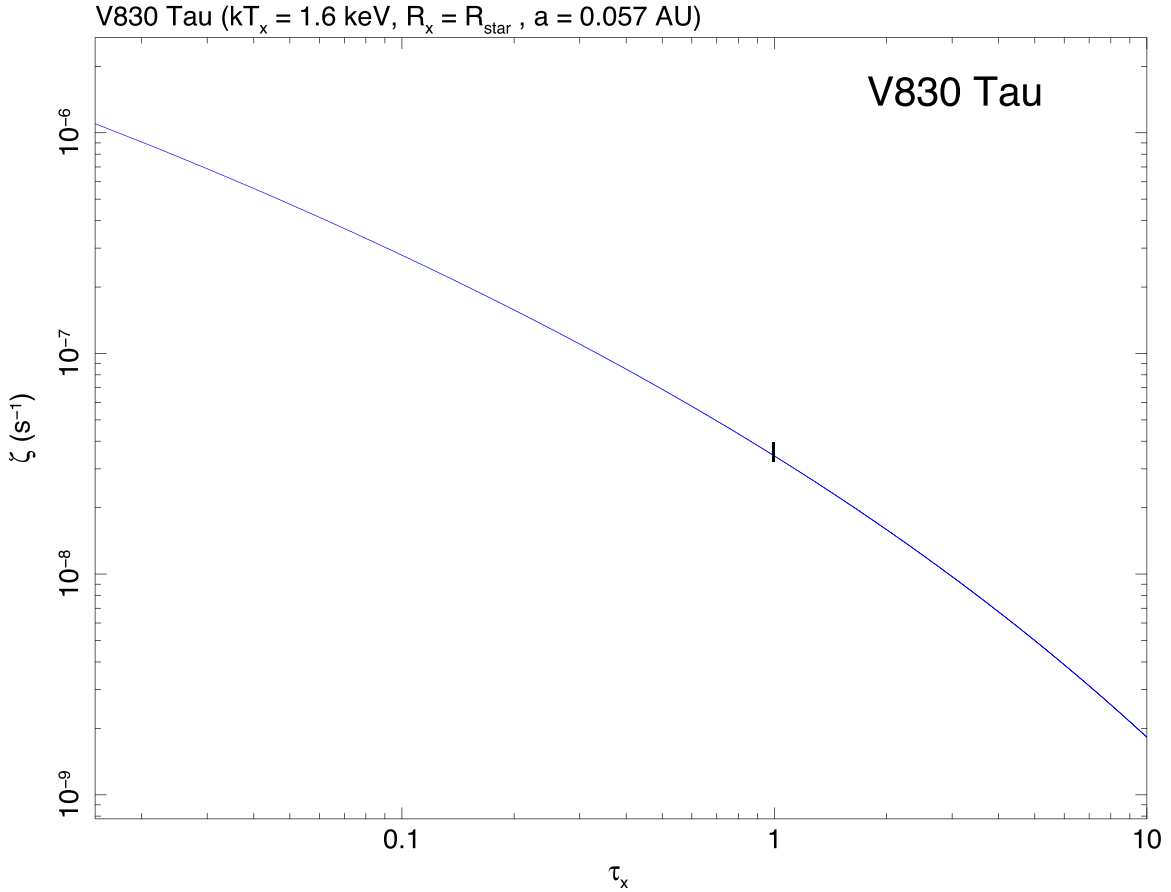
Figure 5. X-ray ionization rate vs. X-ray optical depth computed at at a distance 0.057 au from V830 Tau for a stellar X-ray temperature of $kT_x = 1.6$ keV and luminosity $\log L_x = 30.4$ erg s^{-1} (Equation (1); Table 6).

Table 5
V830 Tau MEG1 Spectral Fit

N_H (cm^{-2})	kT_1 (keV)	kT_2 (keV)	norm$_1$ (cm^{-5})	norm$_2$ (cm^{-5})	Abundances	F_x (erg cm^{-2} s^{-1})	$\log L_x$ (erg s^{-1})
8×10^{20}	0.42 [0.28, 1.23]	2.07 [1.12, 6.34]	14.0×10^{-04}	5.9×10^{-04}	varied[a]	$1.11\ (1.62) \times 10^{-12}$	30.52

Notes. Based on 2T vapec fits of the combined MEG1 spectrum (785 net counts) from all four observations binned to a minimum of 10 counts per bin. The column density N_H was held fixed, and the abundances of Ne, Mg, Si, and Fe were allowed to vary. The abundances of other metals were held fixed at an abundance of $0.4 \times$ solar. Abundances are relative to the solar photospheric values of Anders & Grevesse (1989). Brackets enclose 1σ confidence ranges. The XSPEC *norm* is related to the volume emission measure by EM $= n_e^2 V = 4\pi \times 10^{14} d_{cm}^2 \cdot$norm where n_e is the electron density in the X-ray emitting plasma of volume V and d$_{cm}$ is the source distance in cm. For V830 Tau, $d = 130.4$ pc gives $n_e^2 V = 2.03 \times 10^{42} \cdot$norm. The flux F_x(0.2–8 keV) is the absorbed (observed) value followed in parentheses by the unabsorbed value.
[a] The varied abundances converged to Ne = 0.25 [0.04–0.88], Mg = 0.15 [* - 0.48], Si = 0.23 [0.06–0.58], and Fe = 0.07 [* - 0.33]$\times$ solar. An asterisk denotes no convergence on the lower bound by the error-calculation algorithm.

increasing penetration depth as illustrated in more detail below (see also Cecchi-Pestellini et al. 2006).

We use the analytical development of Shang et al. (2002) to compute the X-ray ionization and heating rates. At a distance r from the star, the total X-ray ionization rate corresponding to a primary ionization rate ζ_x in a thermal plasma at X-ray temperature kT_x is

$$\zeta \approx \zeta_x \left[\frac{r}{R_x} \right]^{-2} \left[\frac{kT_x}{\epsilon_{\rm ion}} \right] I_p(\tau_x) \quad (\text{s}^{-1} \text{ per H nucleus}). \quad (1)$$

In the above, $R_x \geqslant R_*$ sets the distance of the X-ray source above the star, $\epsilon_{\rm ion} \approx 37$ eV is the energy to create an ion pair (i.e., the net energy of the primary photoionized electron $E - E_i$ divided by the number of secondary ionizations it produces), and the function $I_p(\tau_x)$ gives the X-ray attenuation at optical depth $\tau_x(r, E)$, as described in Appendix C of Shang et al. (2002). For X-rays originating in coronal loops, one expects R_x to be a few stellar radii, but for the calculations given below we simply set $R_x = R_* = 2\,R_\odot$. Assuming a planet at separation $r = a = 0.057$ au (Donati et al. 2017) gives $r/R_x = r/R_* = 6.14$.

8
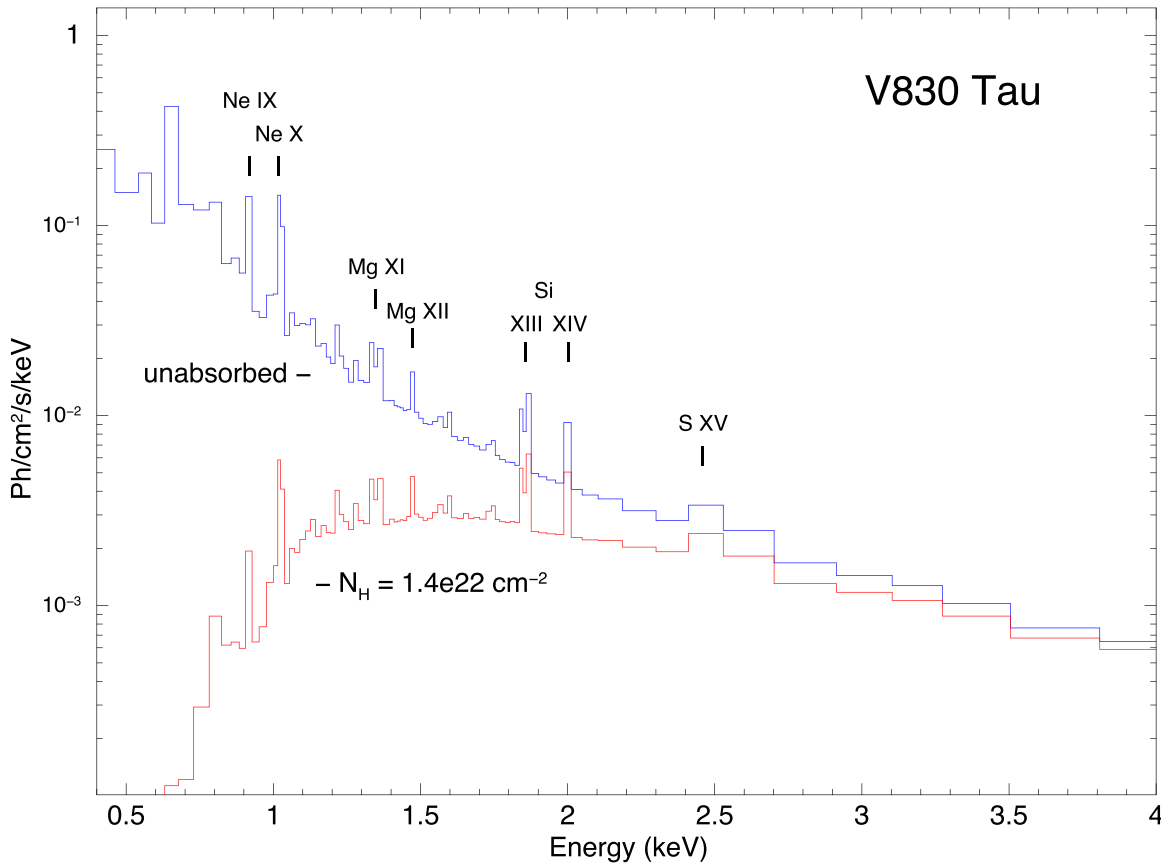
Figure 6. Unfolded Chandra MEG1 spectrum of V830 Tau based on a 2T vapec variable abundance model (Table 5). The unabsorbed ($N_H = 0$) version of the model depicts the shape of the spectrum incident on the planet. The absorbed model ($N_H = 1.4 \times 10^{22}$ cm^{-2}) corresponds to $\tau_x = 1$ at $E = 1.6$ keV and shows low-energy photon absorption by the planet's atmosphere. The photon flux density has been normalized to unity for display purposes.

Table 6
X-ray Ionization and Heating Rates (V830 Tau)

r (au)	kT_x (keV)	ζ_x (s^{-1})	ζ (s^{-1} H^{-1})	τ_x	Γ_x (erg s^{-1} cm^{-3} n_H^{-1})
0.057	1.6	2.83×10^{-07}	3.43×10^{-08}	1	1.10×10^{-18}

Notes. The secondary ionization rate ζ (Equation (1)), primary ionization rate ζ_x (Equation (2)), and heating rate Γ_x (Equation (4)) are computed at $\tau_x = 1$ using $kT = 1.6$ keV, $L_x = 2.5 \times 10^{30}$ erg s^{-1}, $R_x = R_*$, Q = 20 eV, and an assumed planet separation of $r = a = 0.057$ au. The value of n_H required to evaluate Γ_x depends on the adopted planet-atmosphere model and has been left as a free parameter.

The primary X-ray ionization rate is (Shang et al. 2002)

$$\zeta_x = \frac{L_x \sigma(kT_x)}{4\pi R_x^2 kT_x} = 1.13 \times 10^{-8} \left[\frac{L_x}{10^{30} \text{ erg s}^{-1}} \right]$$
$$\times \left[\frac{kT_x}{\text{keV}} \right]^{-(p+1)} \left[\frac{R_x}{10^{12} \text{ cm}} \right]^{-2} \quad (\text{s}^{-1}) \quad (2)$$

where, as above, $\sigma(kT_x) = \sigma(E)$ is the photoelectric X-ray absorption cross section per H nucleus evaluated at energy E. We compute ζ as a function of τ_x at $r = 0.057$ au, adopting a plasma temperature of $kT_x = 1.6$ keV, and log $L_x = 30.4$ erg s^{-1}. The adopted values of kT_x and L_x are representative of the range determined from existing Chandra and XMM-Newton observations of V830 Tau (Table 4; Section 3.1). The

computed ionization rate as a function of τ_x is shown in Figure 5 and the values corresponding to $\tau_x = 1$ at 1.6 keV are given in Table 6. Figure 6 shows a comparison of the incident X-ray spectrum on the planet's atmosphere and the absorbed spectrum at $N_H = 1.4 \times 10^{22}$ cm^{-2} ($\tau_x = 1$ at 1.6 keV).

The X-ray heating rate per unit volume is proportional to the ionization rate and is given by

$$\Gamma_x = \zeta n_H Q \quad (3)$$

where Q is the heating rate per ionization and n_H is the number density of hydrogen nuclei in the planet's atmosphere at the height corresponding to the optical depth τ_x at which ζ was computed (Equation (1)). The value of Q depends on several factors including the nature of the gas (i.e., atomic versus molecular), as discussed by Glassgold et al. (2012). Using a fiducial value of Q = 20 eV gives

$$\Gamma_x = 3.2 \times 10^{-11} \zeta n_H \left[\frac{Q}{20 \text{ eV}} \right] \quad (\text{erg cm}^{-3} \text{ s}^{-1}). \quad (4)$$

The representative value of Γ_x in Table 6 leaves n_H as a free parameter since it depends on the planet's atmospheric structure, about which nothing is yet known.

4.3. EUV Ionization and Heating

EUV photons ($\lambda = 124$–920 Å) have energies of $E = 0.013$–0.1 keV, which are less energetic than X-rays but

still capable of ionizing hydrogen and heating the planet's outer atmosphere. Because of their lower energies, EUV photons are absorbed higher in the atmosphere than X-ray photons. At column densities of $N_H \gtrsim 10^{19}$–10^{20} cm^{-2} the optical depth at EUV energies becomes large and EUV heating is negligible (Cecchi-Pestellini et al. 2009). For TTSs with strong EUV emission there is a balance between EUV photoionization and radiative recombination at optical depths $\tau_{EUV} < 1$, and Lyα cooling in the planet's atmosphere must be taken into account.

The EUV heating rate Γ_{EUV} is computed in a manner similar to that of X-rays (Murray-Clay et al. 2009; Cecchi-Pestellini et al. 2009). For a simplified monoenergetic EUV flux at energy E_0 the heating rate is

$$\Gamma_{EUV} = \epsilon F_{EUV} \sigma(E_0) e^{-\tau_{euv}} n_H \quad (\mathrm{erg\ cm^{-3}\ s^{-1}}) \qquad (5)$$

where ϵ is the fraction of primary photoelectron energy that goes into gas heating, F_{EUV} is the unattenuated EUV energy flux impinging on the planet's atmosphere, $\sigma(E_0)$ is the EUV photoelectric cross section, $\tau_{euv} = \sigma(E_0) N_H$, and n_H is the number density corresponding to N_H at optical depth τ_{euv}. The fractional heating efficiency $\epsilon < 1$ depends on the electron density and values as small as $\epsilon \approx 0.1$–0.2 are possible (Cecchi-Pestellini et al. 2009). The ionization rate $\zeta_{EUV} = F_{EUV} e^{-\tau_{euv}} \sigma(E_0)/E_0$ (s^{-1} per H nucleus) is incorporated into Equation (5).

At distance a from the star $F_{EUV} = L_{EUV}/(4\pi a^2)$. Using $L_x = 2.5 \times 10^{30}$ erg s^{-1} for V830 Tau, Equation (5) evaluated at $a = 0.057$ au can be written as

$$\Gamma_{EUV} = 2.75 \times 10^5 \epsilon \left[\frac{L_{EUV}}{L_x} \right] \sigma(E_0) e^{-\tau_{euv}} n_H \quad (\mathrm{erg\ cm^{-3}\ s^{-1}})$$

$$(6)$$

To numerically compute Γ_{EUV}, the flux F_{EUV} (or equivalently L_{EUV}) must be known. However, stellar EUV fluxes cannot be measured except for the Sun and a few nearby stars because of strong absorption by neutral hydrogen in the interstellar medium. Previous studies have yielded estimates of L_{EUV}/L_x, but with large scatter. For the young solar-type star EK Dra, Ribas et al. (2005) obtained $L_{EUV} \approx L_x$, whereas other studies based on larger samples of stars gave $L_{EUV} \sim$ a few times L_x (e.g., Sanz-Forcada et al. 2011). Methods for estimating L_{EUV} have also been obtained using correlations between L_x and $L_{Ly\alpha}$ (Linsky et al. 2013, 2015). In the absence of an observational measurement some general studies of planetary atmospheres assume $L_{EUV} \sim L_x$ (e.g., Owen & Jackson 2012). Since L_x is variable for V830 Tau we also expect L_{EUV} to vary, as is true even for older, relatively inactive stars like the Sun (Woods et al. 2005).

For the EUV cross section we adopt $\sigma(E = 0.1$ keV$) = 6 \times 10^{-20}$ cm^2 (Bruderer et al. 2009) as a reference value and a profile $\sigma(E) = 6 \times 10^{-20}(E/100$ eV$)^{-p}$ (cm^2) with $p = 2.485$. At a representative EUV energy $E_0 = 60$ eV the cross section is $\sigma(60$ eV$) \approx 2 \times 10^{-19}$ cm^2 and $\tau_{EUV} = 1$ corresponds to $N_H = 5 \times 10^{18}$ cm^{-2}. At this energy the heating rate at unit optical depth becomes $\Gamma_{EUV} = 2 \times 10^{-14} \epsilon [L_{EUV}/L_x] n_H$ (erg cm^{-3} s^{-1}).

4.4. Comments on Planet-Atmosphere Models

Until further observations reconcile the discordant results of RV studies (Section 1) and establish the planet's existence beyond reasonable doubt, detailed atmospheric modeling would be highly speculative and is not yet warranted. However,

we summarize below some relevant factors and limitations that will need to be confronted in any future atmospheric modeling studies.

A realistic atmosphere model requires knowledge of the host star's properties and the planet's separation and physical properties. The separation and relevant properties of V830 Tau itself are now reasonably well known (Table 1), except for its EUV luminosity which must be estimated using indirect methods (Section 4.3). The suspected planet's physical properties are mostly unknown except for a mass estimate and orbital period.

The key quantity needed to calculate the XUV heating rate (Equations (4) and (5)) is $n_H(z)$, the number density versus height z in the planet's atmosphere, where z is typically defined as the distance above a fiducial planet radius R_p (but as already noted, R_p is not known for V830 Tau b). The number density is related to the mass density by the usual expression $n_H = \rho/(\mu m_H)$ where m_H is the mass of hydrogen and μ is the mean weight per particle (amu) in the atmosphere. Not to be overlooked is the dependence of μ on chemical composition and state of the atmospheric gas (molecular, atomic, or ionized). Both the composition and gas state are expected to vary with height, as is known to occur even in the Earth's atmosphere. The chemical composition of hot-Jupiter atmospheres is generally not observationally constrained except for a few well-studied objects like HD 209458 b (Charbonneau et al. 2002; Cody & Sasselov 2002). Thus a H-dominated atmosphere or an H+He mixture is usually assumed, as will probably be necessary for V830 Tau b.

Most current hot-Jupiter atmosphere models are initialized by assuming a base-level density (or pressure) and temperature at a reference height in the atmosphere. The base level ($z = 0$) is often taken to be the planet's radius R_p. The base-level values are then extrapolated upward to obtain the run of temperature (T), pressure (P), or density with height (e.g., Yelle 2004; Murray-Clay et al. 2009; Salz et al. 2016). There is considerable variation in assumed base-level values and simulated T–P profiles even for HD 209458 b (Figure 9 of Vidal-Madjar et al. 2011).

As a first approximation of the base-level temperature the planet's equilibrium temperature can be used, $T_{eq} = T_{eff} [R_*/2a]^{0.5} [f(1-A_B)]^{0.25}$, where A_B is the planet's Bond albedo and $f = 1$ for even heating of the atmosphere (Seager et al. 2000). Using the stellar parameters for V830 Tau (Table 1) and assuming $A_B \approx 0.05$–0.1 for a hot Jupiter (Sudarsky et al. 2000) gives $T_{eq} \approx 1200$ K. This expression accounts for the star's photospheric heating but not XUV heating or any internal planet heating, so it would need to be considered a lower limit for V830 Tau b.

The value to be used for the planet's base density (or pressure) corresponding to the adopted base temperature is quite uncertain. Some guidance is provided by theoretical T–P models of different classes of extrasolar giant planets (e.g., Sudarsky et al. 2003). Uncertainties in the base-level density propagate to higher levels and thereby affect the heating rate at a given height. Heating in the upper atmospheres of hot Jupiters is believed to result in mass loss via a slow planetary wind which must be modeled hydrodynamically (e.g., Yelle 2004; Murray-Clay et al. 2009; Owen & Jackson 2012). In the hydrodynamic picture the mass-loss rate for a steady spherical wind is (Lamers & Cassinelli 1999) $\dot{M}_p = 4\pi r^2 \rho_{wind}(r) v_{wind}(r)^2$, where r is the radial distance from the planet's center, $\rho_{wind}(r)$ is the wind's

mass density, and $v_{\mathrm{wind}}(r)$ is the wind speed. Uncertainties in the base-level density translate into uncertainties in the wind density and $\dot{M}_p$, as discussed by Salz et al. (2016).

5. Summary

1. We have presented new Chandra observations of V830 Tau, a TTS which may host a hot Jupiter. The star's X-ray emission is characterized by multi-temperature plasma viewed through low absorption and is variable. The Chandra observations give an X-ray luminosity of $\log L_x(0.2–8 \mathrm{\ keV}) = 30.10–30.58 \mathrm{\ erg \ s}^{-1}$ but previous XMM-Newton observations reveal values as high as $\log L_x = 30.87 \mathrm{\ erg \ s}^{-1}$.

2. The Chandra MEG1 grating spectrum shows emission lines spanning a range of maximum line power temperatures from Ne IX ($T_{\max} = 4$ MK) to S XV ($T_{\max} = 16$ MK). No significant centroid shifts were detected in the brightest lines (Ne IX and Ne X). The Ne IX triplet intercombination (i) line was not detected and there is no indication of a suppressed forbidden-to-intercombination Ne IX line flux ratio that if present could signify high electron densities. These properties are consistent with variable X-ray emission formed in a magnetically active coronal environment, as is generally found for other weak-lined non-accreting TTSs.

3. Adopting $\log L_x(0.2–8 \mathrm{\ keV}) = 30.40 \mathrm{\ erg \ s}^{-1}$ as a typical value for V830 Tau, the unattenuated X-ray flux at a separation of $a = 0.057$ au of the suspected planet is $F_x(0.2–8 \mathrm{\ keV}) = 2.75 \times 10^5 \mathrm{\ erg \ cm}^{-2} \mathrm{\ s}^{-1}$. This is a factor of $\sim 10^6–10^7$ times greater than the Sun's X-ray flux at Jupiter during active and quiet states.

4. The X-ray ionization and heating rates of the planet's atmosphere were computed based on the star's characteristic X-ray temperature and luminosity. An expression for the EUV heating rate is also given but is subject to uncertainties in the star's EUV luminosity, which is not directly measurable. Numerical values of the X-ray and EUV heating rates depend on the run of number density with height $n_H(z)$ in the planet's atmosphere, which remains to be determined using hydrodynamic models.

5. Detailed atmospheric models will be justified if the planet's existence is firmly established. We have identified several areas of uncertainty that will need to be addressed in any future models. These include unknown or poorly constrained quantities such as the star's EUV luminosity, the planet's radius and chemical composition, and base-level temperature, pressure, and density deep in the atmosphere.

6. Additional X-ray monitoring of V830 Tau would be useful to determine if its X-ray variability is phased to the stellar rotation period or the planet's reported orbital period.

Facility: Chandra X-ray Observatory.

Software: CIAO (Fruscione et al. 2006), XSPEC (Arnaud 1996).

ORCID iDs

Stephen L. Skinner ● https://orcid.org/0000-0002-3025-3055
Manuel Güdel ● https://orcid.org/0000-0001-9818-0588

References

Akeson, R. L., Boden, A. F., Monnier, J. D., et al. 2005, ApJ, 635, 1173
Anders, E., & Grevesse, N. 1989, Geochim. Cosmochim. Acta, 53, 197
Arnaud, K. A. 1996, in ASP Conf. Ser. 101, Astronomical Data Analysis Software and Systems V, ed. G. Jacoby & J. Barnes (San Francisco, CA: ASP), 17
Bower, G. C., Loinard, L., Dzib, S., et al. 2016, ApJ, 830, 107
Bruderer, S., Doty, S. D., & Benz, A. O. 2009, ApJS, 183, 179
Cecchi-Pestellini, C., Ciaravella, A., & Micela, G. 2006, A&A, 458, L13
Cecchi-Pestellini, C., Ciaravella, A., Micela, G., & Penz, T. 2009, A&A, 496, 863
Charbonneau, D., Brown, T. M., Noyes, R. W., & Gilliland, R. L. 2002, ApJ, 568, 377
Cody, A. M., & Sasselov, D. D. 2002, ApJ, 569, 451
Damasso, M., Lanza, A. F., Benatti, S., et al. 2020, A&A, 642, A133
Dawson, R. I., & Johnson, J. A. 2018, ARA&A, 56, 175
Donati, J.-F., Hébrard, E., Hussain, G. A. J., et al. 2015, MNRAS, 453, 3706
Donati, J.-F., Moutou, C., Malo, L., et al. 2016, Natur, 534, 662
Donati, J.-F., Yu, L., Moutou, C., et al. 2017, MNRAS, 465, 3343
Franciosini, E., Pillitteri, I., Stelzer, B., et al. 2007, A&A, 468, 485
Fruscione, A., McDowell, J. C., Allen, G. E., et al. 2006, Proc. SPIE, 6270, 62701V
Getman, K. V., Feigelson, E. D., Broos, P. S., Micela, G., & Garmire, G. P. 2008, ApJ, 688, 418
Glassgold, A. E., Galli, D., & Padovani, M. 2012, ApJ, 756, 157
Glassgold, A. E., Najita, J., & Igea, J. 1997, ApJ, 480, 344
Gorenstein, P. 1975, ApJ, 198, 95
Grankin, K. N., Bouvier, J., Herbst, W., & Melnikov, S. Y. 2008, A&A, 479, 827
Güdel, M., Briggs, K. R., Arzner, K., et al. 2007, A&A, 468, 353
Herczeg, G. J., & Hillenbrand, L. A. 2014, ApJ, 786, 97
Igea, J., & Glassgold, A. E. 1999, ApJ, 518, 848
Imanishi, K., Nakajima, H., Tsujimoto, M., Koyama, K., & Tsuboi, Y. 2003, PASJ, 55, 653
Kraus, A. L., & Ireland, M. J. 2012, ApJ, 745, 5
Lamers, H. J. G. L. M., & Cassinelli, J. P. 1999, Introduction to Stellar Winds (Cambridge: Cambridge Univ. Press), 60
Linsky, J. L., France, K., & Ayres, T. 2013, ApJ, 766, 69
Linsky, J. L., France, K., & Ayres, T. 2015, in Proc. of XVIII Cambridge Workshop on Cool Stars, Stellar Systems, and the Sun, 831, ed. G. T. van Belle & H. C. Harris (Flagstaff, AZ: Lowell Observatory)
Mayor, M., & Queloz, D. 1995, Natur, 378, 355
Murray-Clay, R. A., Chiang, E. I., & Murray, N. 2009, ApJ, 693, 23
Owen, J. E., & Jackson, A. P. 2012, MNRAS, 425, 2931
Poppenhaeger, K., Robrade, J., & Schmitt, J. H. M. M. 2010, A&A, 515, A98
Ribas, I., Guinan, E. F., Güdel, M., & Audard, M. 2005, ApJ, 622, 680
Sallum, S., Follette, K. B., Eisner, J. A., et al. 2015, Natur, 527, 342
Salz, M., Czesla, S., Schneider, P. C., & Schmitt, J. H. M. M. 2016, A&A, 586, A75
Sanz-Forcada, J., Micela, G., Ribas, I., et al. 2011, A&A, 532, A6
Seager, S., Whitney, B. A., & Sasselov, D. D. 2000, ApJ, 540, 504
Shang, H., Glassgold, A. E., Shu, F. H., & Lizano, S. 2002, ApJ, 564, 853
Skinner, S. L., & Güdel, M. 2013, ApJ, 765, 3
Skinner, S. L., & Güdel, M. 2017, ApJ, 839, 45
Smith, R. K., Brickhouse, N. S., Liedahl, D. A., & Raymond, J. C. 2001, ApJ, 556, L91
Strugarek, A., Bolmont, E., Mathis, S., et al. 2017, ApJL, 847, L16
Sudarsky, D., Burrows, A., & Hubeny, I. 2003, ApJ, 588, 1121
Sudarsky, D., Burrows, A., & Pinto, P. 2000, ApJ, 538, 885
Telleschi, A., Güdel, M., Briggs, K. R., Audard, M., & Palla, F. 2007, A&A, 468, 425
Vidal-Madjar, A., Sing, D. K., Lecavelier des Etangs, A., et al. 2011, A&A, 527, A110
Vuong, M. H., Montmerle, T., Grosso, N., et al. 2003, A&A, 408, 581
Woods, T. N., Eparvier, F. G., Bailey, S. M., et al. 2005, JGR, 110, A01312
Yelle, R. V. 2004, Icar, 170, 167
Yu, L., Donati, J.-F., Hébrard, E. M., et al. 2017, MNRAS, 467, 1342